LETTER TO THE EDITOR

Ordered magnetic fields around the 3C 84 central black hole

G. F. Paraschos[1], J.-Y. Kim[2,1], M. Wielgus[1,3], J. Röder[1], T. P. Krichbaum[1], E. Ros[1], I. Agudo[4],
I. Myserlis[5,1], M. Moscibrodzka[6], E. Traianou[4,1], J. A. Zensus[1], L. Blackburn[7,8], C.-K. Chan[9,10,11], S. Issaoun[8,12],
M. Janssen[6,1], M. D. Johnson[7,8], V. L. Fish[13], K. Akiyama[13,14,7], A. Alberdi[4], W. Alef[1], J. C. Algaba[15],
R. Anantua[7,8,16], K. Asada[17], R. Azulay[18,19,1], U. Bach[1], A.-K. Baczko[20,1], D. Ball[9], M. Baloković[21], J. Barrett[13],
M. Bauböck[22], B. A. Benson[23,24], D. Bintley[25,26], R. Blundell[8], K. L. Bouman[27], G. C. Bower[28,29], H. Boyce[30,31],
M. Bremer[32], C. D. Brinkerink[6], R. Brissenden[7,8], S. Britzen[1], A. E. Broderick[33,34,35], D. Broguiere[32],
T. Bronzwaer[6], S. Bustamante[36], D.-Y. Byun[37,38], J. E. Carlstrom[39,24,40,41], C. Ceccobello[20], A. Chael[42],
D. O. Chang[7,8], K. Chatterjee[7,8], S. Chatterjee[43], M. T. Chen[28], Y. Chen[44,45] (陈永军), X. Cheng[37], I. Cho[4],
P. Christian[46], N. S. Conroy[47,8], J. E. Conway[20], J. M. Cordes[43], T. M. Crawford[24,39], G. B. Crew[13],
A. Cruz-Osorio[48,49], Y. Cui[50,51], R. Dahale[4], J. Davelaar[52,53,6], M. De Laurentis[54,49,55], R. Deane[56,57,58],
J. Dempsey[25,26,59], G. Desvignes[1,60], J. Dexter[61], V. Dhruv[22], S. S. Doeleman[7,8], S. Dougal[9], S. A. Dzib[32,1],
R. P. Eatough[62,1], R. Emami[8], H. Falcke[6], J. Farah[63,64], E. Fomalont[65], H. A. Ford[9], M. Foschi[4],
R. Fraga-Encinas[6], W. T. Freeman[66,67], P. Friberg[25,26], C. M. Fromm[68,49,1], A. Fuentes[4], P. Galison[7,69,70],
C. F. Gammie[22,47,71], R. García[32], O. Gentaz[32], B. Georgiev[34,35,33], C. Goddi[72,73,74,75], R. Gold[76],
A. I. Gómez-Ruiz[77,78], J. L. Gómez[4], M. Gu (顾敏峰)[44,79], M. Gurwell[8], K. Hada[80,81], D. Haggard[30,82],
K. Haworth[8], M. H. Hecht[13], R. Hesper[83], D. Heumann[9], L. C. Ho[84,85], P. Ho[17,26,25], M. Honma[80,81,86],
C. L. Huang[17], L. Huang[44,79], D. H. Hughes[77], S. Ikeda[14,87,88,89], C. M. V. Impellizzeri[90,65], M. Inoue[17],
D. J. James[91,92], B. T. Jannuzi[9], B. Jeter[17], W. Jaing (江悟)[44], A. Jiménez-Rosales[6], S. Jorstad[93], A. V. Joshi[22],
T. Jung[37,38], M. Karami[33,34], R. Karuppusamy[1], T. Kawashima[94], G. K. Keating[8], M. Kettenis[95], D.-J. Kim[1],
J. Kim[37], J. Kim[27], M. Kino[14,96], J. Y. Koay[17], P. Kocherlakota[49], Y. Kofuji[80,86], P. M. Koch[17], S. Koyama[97,17],
C. Kramer[32], J. A. Kramer[1], M. Kramer[1], C.-Y. Kuo[98,17], N. La Bella[6], T. R. Lauer[99], D. Lee[22], S.-S. Lee[37],
P. K. Leung[100], A. Levis[27], Z. Li[101,102], R. Lico[103,4], G. Lindahl[8], M. Lindqvist[20], M. Lisakov[1], J. Liu[1], K. Liu[1],
E. Liuzzo[104], W.-P. Lo[17,105], A. P. Lobanov[1], L. Loinard[106,48], C. J. Lonsdale[13], A. E. Lowitz[9], R.-S. Lu[44,45,1],
N. R. MacDonald[1], J. Mao[107,108,109], N. Marchili[104,1], S. Markoff[110,111], D. P. Marrone[9], A. P. Marscher[93],
I. Martí-Vidal[18,19], S. Matsushita[17], L. D. Matthews[13], L. Medeiros[112,12], K. M. Menten[1], D. Michalik[113,24],
I. Mizuno[25,26], Y. Mizuno[51,114,49], J. M. Moran[7,8], K. Moriyama[49,13,80], W. Mulaudzi[110], C. Müller[1,6], H. Müller[1],
A. Mus[18,19], G. Musoke[110,6], A. Nadolski[47], H. Nagai[14,81], N. M. Nagar[115], M. Nakamura[116,17], G. Narayanan[36],
I. Natarajan[8,7], A. Nathanail[117,49], S. Navarro Fuentes[5], J. Neilsen[118], R. Neri[32], C. Ni[34,35,33], A. Noutsos[1],
M. A. Nowak[119], J. Oh[95], H. Okino[80,86], H. Olivares[6], G. N. Ortiz-León[77,1], T. Oyama[80], F. Özel[120],
D. C. M. Palumbo[7,8], J. Park[121], H. Parsons[25,26], N. Patel[8], U.-L. Pen[17,33,122,123,124], V. Piétu[32], R. Plambeck[125],
A. PopStefanija[36], O. Porth[110,49], F. M. Pötzl[126,1], B. Prather[22], J. A. Preciado-López[33], D. Psaltis[120],
H.-Y. Pu[127,128,17], V. Ramakrishnan[115,129,130], R. Rao[8], M. G. Rawlings[131,24,26], A. W. Raymond[7,8],
L. Rezzolla[49,132,133], A. Ricarte[8,7], B. Ripperda[122,134,123,33], F. Roelofs[8,7,6], A. Rogers[13], C. Romero-Cañizales[17],
A. Roshanineshat[9], H. Rottmann[1], A. L. Roy[1], I. Ruiz[5], C. Ruszczyk[13], K. L. J. Rygl[104], S. Sánchez[5],
D. Sánchez-Argüelles[77,78], M. Sánchez-Portal[5], M. Sasada[135,80,136], K. Satapathy[9], T. Savolainen[137,131,1],
F. P. Schloerb[36], J. Schonfeld[8], K. Schuster[32], L. Shao[85,1], Z. Shen[44,45], D. Small[95], B. W. Sohn[37,38,138],
J. SooHoo[13], L. D. Sosapanta Salas[110], K. Souccar[36], H. Sun[139,140], F. Tazaki[80], A. J. Tetarenko[141], P. Tiede[8,7],
R. P. J. Tilanus[9,6,90,142], M. Titus[13], P. Torne[5,1], T. Toscano[4], T. Trent[9], S. Trippe[143], M. Turk[47], I. van Bemmel[95],
H. J. van Langevelde[95,90,144], D. R. van Rossum[6], J. Vos[6], J. Wagner[1], D. Ward-Thompson[145], J. Wardle[146],
J. E. Washington[9], J. Weintroub[7,8], R. Wharton[1], K. Wiik[147], G. Witzel[1], M. F. Wondrak[6,148], G. N. Wong[149,42],
Q. Wu[150], N. Yadlapalli[27], P. Yamaguchi[8], A. Yfantis[6], D. Yoon[110], A. Young[6], K. Young[8], Z. Younsi[151,49], W. Yu[8],
F. Yuan[44,79,152], Y.-F. Yuan[153], S. Zhang[154], G. Y. Zhao[4], and S.-S. Zhao[44]

(Affiliations can be found after the references)

ABSTRACT

Context. 3C 84 is a nearby radio source with a complex total intensity structure, showing linear polarisation and spectral patterns. A detailed investigation of the central engine region necessitates the use of very-long-baseline interferometry (VLBI) above the hitherto available maximum frequency of 86 GHz.

Aims. Using ultrahigh resolution VLBI observations at the currently highest available frequency of 228 GHz, we aim to perform a direct detection of compact structures and understand the physical conditions in the compact region of 3C 84.

Methods. We used Event Horizon Telescope (EHT) 228 GHz observations and, given the limited (u, v)-coverage, applied geometric model fitting to the data. Furthermore, we employed quasi-simultaneously observed, ancillary multi-frequency VLBI data for the source in order to carry out a comprehensive analysis of the core structure.

Results. We report the detection of a highly ordered, strong magnetic field around the central, supermassive black hole of 3C 84. The brightness temperature analysis suggests that the system is in equipartition. We also determined a turnover frequency of $\nu_m = (113 \pm 4)$ GHz, a corresponding synchrotron self-absorbed magnetic field of $B_{SSA} = (2.9 \pm 1.6)$ G, and an equipartition magnetic field of $B_{eq} = (5.2 \pm 0.6)$ G. Three components are resolved with the highest fractional polarisation detected for this object ($m_{net} = (17.0 \pm 3.9)\%$). The positions of the components are compatible with those seen in low-frequency VLBI observations since 2017–2018. We report a steeply negative slope of the spectrum at 228 GHz. We used these findings to test existing models of jet formation, propagation, and Faraday rotation in 3C 84.

Conclusions. The findings of our investigation into different flow geometries and black hole spins support an advection-dominated accretion flow in a magnetically arrested state around a rapidly rotating supermassive black hole as a model of the jet-launching system in the core of 3C 84. However, systematic uncertainties due to the limited (u, v)-coverage, however, cannot be ignored. Our upcoming work using new EHT data, which offer full imaging capabilities, will shed more light on the compact region of 3C 84.

keywords. techniques: high angular resolution – techniques: interferometric – galaxies: active – galaxies: individual: NGC 1275 – galaxies: jets

1. Introduction

The formation of relativistic astrophysical jets is a manifestation of the activity of accreting supermassive black holes residing in the nuclei of galaxies. Such jets can have an immense impact on their surroundings, either by stunting or enhancing the evolution of their host galaxy. Despite substantial efforts dedicated to understanding the physics governing jets, a number of open questions remain, including questions relating to the launching mechanism of these jets. The radio source 3C 84 (NGC 1275; D_L = 78.9 ± 2.4 Mpc, z = 0.0176, Strauss et al. 1992, corresponding to a conversion factor ψ = 0.36 pc mas^{-1}; see also Sect. 2.1) is a nearby active galactic nucleus (AGN) and one of a handful of objects for which the jet formation zone can be resolved and probed with very-long-baseline interferometry (VLBI). Thus, 3C 84 is an ideal test bed for distinguishing between jet-launching models based on the resulting predictions for observables such as magnetic field strength. Using the unique polarimetric 1.3 mm VLBI observations of 3C 84, conducted with the Event Horizon Telescope (EHT; see The Event Horizon Telescope Collaboration 2019a, 2022a), we are now able to distinguish between such models.

According to the current understanding, the linear polarisation is present in both the downstream jet (Nagai et al. 2017) and the compact region (Kim et al. 2019) of 3C 84, although its amplitude is low. A quantitative characterisation of the location of the 1.3 mm polarisation within the jet flow is crucial in order to distinguish between the different jet-launching models. To illustrate this, an interesting comparison can be made between the jet collimation near the jet base in M 87 (exhibiting a narrower opening angle, as seen, e.g., in Kim et al. 2018) and 3C 84 (featuring instead a wide structure as seen by *RadioAstron* and reported in Giovannini et al. 2018). Given this elongated structure, a disc-launched jet (Blandford & Payne 1982) threaded by toroidal magnetic field lines is a possible explanation. The alternative scenario is the more commonly invoked black hole launched jet (Blandford & Znajek 1977) associated with poloidal magnetic field lines. Polarimetry at 1.3 mm is less affected by opacity effects and can

therefore be used to test the necessary conditions for different jet-launching scenarios, as presented in this work. We therefore employed high-resolution millimetre VLBI to investigate how the substantial increase in polarisation with frequency in 3C 84 can be explained by the prevalent magnetic field.

2. Data, analysis, and results

2.1. Data description and analysis

In this work, we examined the first total intensity and polarimetric VLBI observations of 3C 84 at 228 GHz taken with the Event Horizon Telescope (EHT) and compared them with quasi-simultaneous VLBI observations at lower frequencies. 3C 84 was observed during the EHT 2017 campaign (The Event Horizon Telescope Collaboration 2019a, 2022a) at 228 GHz on April 7 between 18:30 and 19:40 UTC, with six scans each around 5 min in length. Five telescopes at three geographical sites participated in the observation: Atacama Large Millimeter/submillimeter Array (ALMA, observing as a phased array; see Goddi et al. 2019) and the Atacama Pathfinder Experiment (APEX) telescope in Chile; the Submillimeter Telescope (SMT) in Arizona; and the *James Clerk Maxwell* Telescope (JCMT) and the Submillimeter Array (SMA) in Hawai'i. Following the correlation, observations were subjected to the standard EHT data reduction path (The Event Horizon Telescope Collaboration 2019b,c, 2022b), including the `EHT-HOPS` fringe-fitting and post-processing pipeline (Blackburn et al. 2019, see also Janssen et al. (2019) for an alternative pipeline used with the EHT data). Additional comments on the data reduction are given in Appendix A. The single-dish data used in this paper were observed by the POLAMI (Thum et al. 2008; Agudo et al. 2018) and QUIVER (Myserlis et al. 2018; Kraus et al. 2003) programmes on April 4 and April 8, 2017, respectively.

As 3C 84 exhibits a low jet expansion velocity inside the submilliarcsecond (submas) region, we are able to use quasi-simultaneous VLBI observations of 3C 84 taken in March and April, 2017, at 15, 43, and 86 GHz to complement our analysis

and assist our interpretation of the underlying jet physics without suffering from time-variability effects. Here, we define as compact region the entire region probed by the long EHT baselines, with an angular size of smaller than 200 µas. Specifically, we used the publicly available Very Long Baseline Array (VLBA) epochs from April 22, 2017 at 15 GHz (MOJAVE monitoring program; see Lister et al. 2018, for details regarding the calibration and imaging procedures) and April 16, 2017 at 43 GHz (VLBA-BU-BLAZAR monitoring program; see Jorstad et al. 2017, for details regarding the calibration and imaging procedures). As both monitoring programs publish fully calibrated and imaged data sets, we opted to use them as provided.

At 86 GHz, we used the Global Millimeter VLBI Array (GMVA) epoch from March 30, 2017 (see Paraschos et al. 2022b, for details regarding the calibration and imaging procedures). The antenna instrumental polarisation calibration (D-terms) was performed using the software polsolve (Martí-Vidal et al. 2021) and the data were imaged using the CLEAN algorithm (see e.g., Shepherd et al. 1994, 1995). The combined (u, v)-coverage of our multi-wavelength observations is shown in Fig. 1.

For our analysis we assumed a BH mass of $M_\bullet = 8 \times 10^8 \, M_\odot$ (Scharwächter et al. 2013), for which 100 µas corresponds to $\sim$500 R_s ($\sim$800 R_s deprojected). We used $H_0 = 69.6$ and $\Omega_M = 0.286$ in a flat cosmology (Bennett et al. 2014), yielding a length scale of $\psi = 0.36$ pc mas^{-1}. Hence, $250 \, R_s \approx 54$ µas ≈ 0.02 pc (0.032 pc de-projected) at $z = 0.0176$.

2.2. Results

We find evidence of a highly ordered, strong magnetic field in the submas compact region of 3C 84. This region is best fitted by three circular Gaussian components, labelled core ('C'), east ('E'), and west ('W'), as shown in Fig. 2 (the method we used is described in Appendix B). The extended flux density detected on the short ALMA-APEX and JCMT-SMA baselines, while resolved out on all long EHT baselines, was fitted by a $\sim$5000 microarcseconds (µas) circular Gaussian component with a flux density of $S_{\text{core}}^{228 \, \text{GHz}} \sim 6.4$ Jy. Furthermore, by averaging[1] the linear fractional polarisation measurements of these three components, we determined the net linear fractional polarisation in the compact region to be $m_{\text{net}} = (17.0 \pm 3.9)\%$. The short baseline between ALMA and APEX yielded an estimate for the linear fractional polarisation on larger arcsecond scales, of $\sim$6% (denoted in the bottom panel of Fig. 3 with the grey marker).

We cross-referenced the submas compact region model fit components at lower frequencies following the method detailed in Savolainen et al. (2008) and Appendix C. While at 15 GHz the submas region appears fully blended, we are able to recover the 228 GHz structure at 86 GHz and even at 43 GHz. The results are reported in Table A.1.

We also measured both the total intensity I and linearly polarised emission P in the submas region of 3C 84 in the 15, 43, and 86 GHz images. The values of linear fractional polarisation at these three lower frequencies are considered as upper limit estimates. The results are shown in Fig. 3. The VLBI total intensity increases up to the 86 GHz measurement, and then decreases towards 228 GHz.

Close-in-time single-dish measurements at 8, 86, and 228 GHz are also shown in Fig. 3 (see also Table A.2). The 86 GHz flux density is higher than that at 228 GHz.

---

[1] We used the formula $100\% \times |\sum(Q + \iota U)| / \sum I$, with I, Q, and U being the image domain Stokes parameters, and performed the pixel-wise summation over the whole field of view.
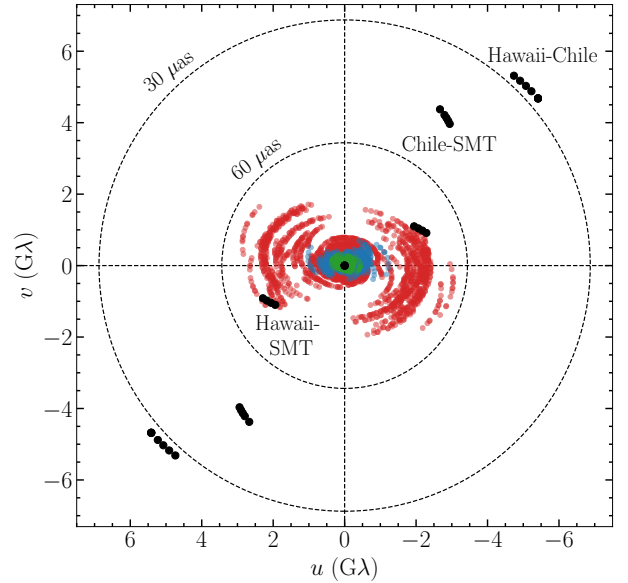

Fig. 1. (u, v)-coverage of 3C 84, as observed with the VLBA (15 GHz, green), VLBA (43 GHz, blue), GMVA (86 GHz, red), and EHT (228 GHz, black). Dashed circles indicate fringe spacings characterising the instrumental resolution of 60 µas and 30 µas. 'Chile' denotes stations ALMA and APEX. 'Hawaii' denotes stations SMA and JCMT. With the higher frequency observations and longer baselines of the EHT, we improve the angular resolution by a factor of >2.

However, the 8 GHz measurement is also higher than at 86 GHz, suggesting a significant contribution from the parsec-scale jet. Furthermore, at 228 GHz, the compact-scale VLBI flux density is significantly lower than the corresponding extended flux density, as long EHT baselines over-resolve the large-scale jet emission structure (similar to M 87, see e.g., The Event Horizon Telescope Collaboration 2019d). In terms of fractional polarisation, it is evident that there is a significant increase at 228 GHz, indicating a transition in the accretion flow to the optically thin regime.

3. Discussion

3.1. Insights from the synchrotron spectrum

Our analysis shows that the east–west elongated core structure (Giovannini et al. 2018) also persists at 1.3 mm, and in lower frequencies (as reported at 7 mm by Punsly et al. 2021 and 3 mm by Oh et al. 2022). Interpretation of the nature of the components comprising this broad core structure heavily depends on the uncertain jet viewing angle (ξ). An upper limit of $\xi \sim 40°$ was reported by Oh et al. (2022) based on a VLBI analysis of the compact region, but much lower values have also been found, for example based on γ-ray analysis (Abdo et al. 2009). The historically subluminal jet component velocities in the compact region (Punsly et al. 2021; Hodgson et al. 2021; Paraschos et al. 2022b) point towards an increased viewing angle. Moreover, different parts of the jet have been reported to be moving with different velocities, which is related to the so-called 'Doppler crisis' phenomenon (e.g., Henri & Saugé 2006) and jet stratification (Nagai et al. 2014).

The high-resolution, high-frequency EHT observation enables a novel diagnosis of the state of plasma surrounding the central black hole via calculation of the turnover frequency ν_m and the synchrotron self-absorption magnetic field
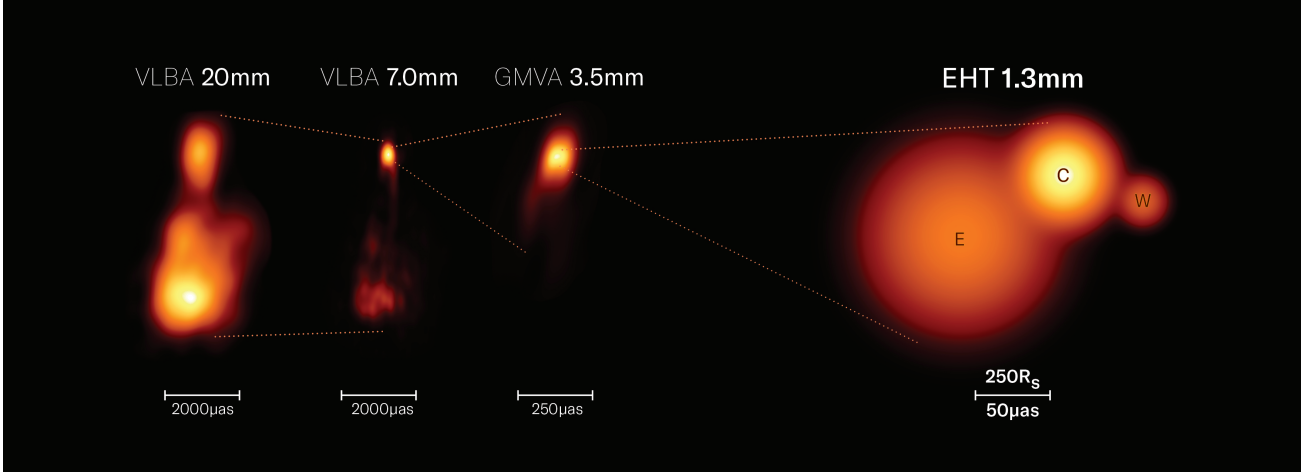
Fig. 2. Total intensity jet morphology of 3C 84 at different wavelengths. From left to right, we display the 15, 43, 86 (images), and 228 GHz (model) measurements. The horizontal line below each image represents the angular scale. The effective beam sizes, corresponding to these observations are, from left to right, 0.40×0.60 mas, 0.34×0.16 mas, 0.11×0.04 mas, and 107×14 μas. R_S denotes the Schwarzschild radius.

strength B_{SSA}. Assuming ν_m to be 86 GHz, Hodgson et al. (2018) and Kim et al. (2019) computed the B_{SSA} to be ~21 G. Using additional EHT flux density measurements, we can directly measure ν_m. While the different observations correspond to different (u, v) coverages, we fitted a focused Gaussian model to the high-signal-to-noise ratio (S/N) data at 228 GHz, finding core diameters within the order of magnitude of the diffraction limit. We also fixed the sizes of the components for all the frequencies in order to mitigate the effects of the different (u, v) coverages (see Table A.1). Subsequently, fitting, then, Eq. (5.90) from Condon & Ransom (2016) (see also Rybicki & Lightman 1979 and Appendix D) to the data yields $\nu_m = (113 \pm 4)$ GHz (see also Türler et al. 2000). We computed a core brightness temperature of $T_B = (3.6 \pm 1.5) \times 10^{11}$ K from ν_m, assuming that the angular size of the components at ν_m is the same as at 228 GHz (as the system is optically thin at both frequencies). Within the error budget, the system seems to be in equipartition (Singal 1986) between kinetic and magnetic energies (also reported by Paraschos et al. 2023, based on light-curve variability analysis).

Furthermore, we computed $B_{SSA} = (2.9 \pm 1.6)$ G using Eq. (2) from Marscher (1983) (see also Appendix D). We also calculated an equipartition magnetic field strength of $B_{eq} = (5.2 \pm 0.6)$ G. The uncertainties were calculated through standard error propagation. The two values agree with each other within the error budget. Our results also tentatively agree within the error budget with the magnetic field reported by Kim et al. (2019). The equipartition Doppler factor is $\delta_{eq} = 1.5 \pm 0.4$, suggesting that the acceleration happens further downstream, which is in line with lower frequency observations of 3C 84 (e.g., Hodgson et al. 2018; Paraschos et al. 2022b, and references therein).

Moreover, the equipartition magnetic field strength B_{eq} in the vicinity of the jet apex was computed to reach up to 4 G in a core shift analysis carried out by Paraschos et al. (2021). However, the magnetic field value mentioned by these latter authors was calculated at the distance between the extrapolated jet apex and the 86 GHz core, resulting in a slightly lower estimate than that found in this work. Nevertheless, it is important to exercise caution when interpreting both ν_m and B_{SSA}. 3C 84 is a variable source (recently up to 20–30% variation in total intensity and linear polarised flux density at 43 GHz within a year based on the monitoring program VLBA-BU-BLAZAR), which means that these observables might be time dependent (compare with the spectrum shown in, e.g., Hodgson et al. 2018). Moreover, our

models still contain large uncertainties due to the sparsity of the (u, v) coverage, which may not be fully accounted for.

3.2. Model interpretation

Possible interpretations of the physical mechanisms driving the wide core structure largely depend on the exact location of the central engine with regard to the observed core. The current understanding is that the central engine is located north or northwest of the 86 GHz VLBI core (Giovannini et al. 2018; Paraschos et al. 2021). As its exact location is still ambiguous, it is unclear whether or not some of the identified components in this work correspond to the core (Case I) or a counter-jet (Case II).

Simulations of the radio jet of M 87 (Mościbrodzka et al. 2017) show that the linear polarisation is produced inside the approaching jet, while the dense accretion disc depolarises any radiation reaching us from the counter-jet. In 3C 84, circumnuclear free-free absorption has already been reported for example by Walker et al. (2000), who cite a possible connection to the accretion disc. It is thought that the presence of this disc obscures the counter-jet in the milliarcsecond (mas) region of 3C 84, which only becomes visible at a distance of >2 mas at higher frequencies (as reported e.g., in Wajima et al. 2020 at 86 GHz). As both E and W in Fig. B.1 are highly linearly polarised (20–80%), this points towards Case I, meaning that the two components might be at the origin of the double-rail structure seen on larger scales, as opposed to a jet and counter-jet geometry. However, we note that this interpretation remains speculative, given the uncertainties.

This high fractional polarisation in E and W could be evidence for highly ordered magnetic field lines in the jet plasma with almost no Faraday depolarisation present. On the other hand, C has lower fractional polarisation and the synchrotron opacity should be nearly negligible at 228 GHz according to the Stokes I spectrum shown in Fig. 3. This may indicate that the main source of depolarisation in the compact region probed by the EHT is beam depolarisation of complex magnetic field patterns or mild Faraday depolarisation, rather than opacity effects. Consequently, a possible Faraday screen located in the compact region could be at most the size of C, which is ~20 μas. However, it should be noted here that W is the most uncertain low-total-intensity component, hindering a reliable conclusion about its nature (see also Appendices A and B).
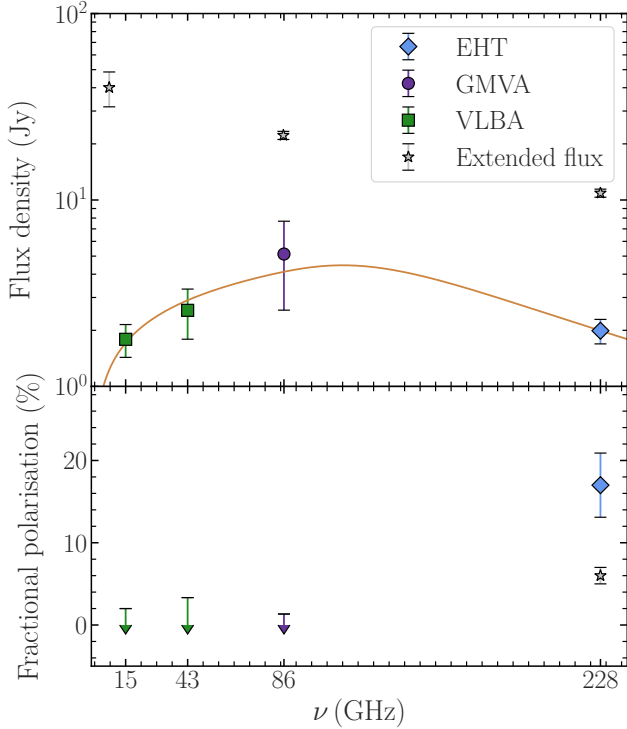
Fig. 3. VLBI and single-dish total intensity and fractional polarisation versus frequency for 3C 84, observed in March and April 2017. *Top*: green box markers, purple dot, and light blue diamond denote the total intensity, compact-scale VLBI flux density measurements at 15, 43, 86, and 228 GHz, respectively. The latter data point is the sum of components *E*, *C*, and *W* (see Table A.1). The orange line denotes the fit to the spectrum using Eq. (D.1). The grey star markers denote the single-dish (extended) flux density measurements at 8 (QUIVER), 86, and 228 GHz (POLAMI). The turnover frequency is between 86 and 228 GHz. The 8 GHz single-dish flux density is higher than at 86 GHz, because the parsec-scale jet flux density contributes to the measurement. *Bottom*: green and purple arrows indicate the upper limits of the fractional polarisation at 15, 43, and 86 GHz measured in the same region as the total intensity values in the upper panel. The light blue diamond marker again indicates the EHT measurement at 228 GHz. The grey star marker indicates the zero-baseline fractional polarisation on the baseline between ALMA and APEX. Error bars in both panels indicate the 68% confidence level.

3C 84 is known to show high amounts of Faraday rotation (RM) and the presence of circular polarisation (see e.g., the POLAMI and QUIVER programmes as described in Agudo et al. 2018; Myserlis et al. 2018, respectively). Using the SMA and CARMA, Plambeck et al. (2014) reported an RM of as high as $\sim 9 \times 10^5$ rad m^{-2}, indicative of the presence of a strong magnetic field. This places 3C 84 in a small group of known radio sources exhibiting similarly high RMs, such as Sgr A* ($\sim 5 \times 10^5$ rad m^{-2}; Wielgus et al. 2022 and references therein), M 87 ($\sim 10^5$ rad m^{-2}; Goddi et al. 2021), and PKS 1830-211 ($\sim 10^8$ rad m^{-2}; Martí-Vidal et al. 2015). However, whether this RM occurs in the medium surrounding the jet (e.g. from a disc wind) or is connected to the accretion flow remains unknown. The origin of the RM can be explored by determining its dependence on the observing frequency (Plambeck et al. 2014; Goddi et al. 2021) or the distance from the central engine (Park et al. 2015).

The density of the accretion flow, which is a related quantity that can be estimated via the RM, is required in order to constrain the mass-accretion rate around BHs (see Nagai et al. 2017, for a relevant discussion about 3C 84) for different accre-

tion flow models, such as advection-dominated accretion flows (ADAFs; see Narayan & Yi 1995) and convection-dominated accretion flows (CDAFs; see Narayan et al. 2000).

Different plausible depolarisation mechanisms have been proposed for 3C 84, that is, originating from such an accretion flow and the jet itself (Li et al. 2016; Kim et al. 2019). Combining the single-dish data presented in Fig. 3, which were taken quasi-simultaneously with the EHT observations, allows us to estimate an estimate of the RM present in 3C 84. We find that RM = $(6.06 \pm 0.01) \times 10^6$ rad m^{-2} by determining the gradient of the EVPAs as a function of the wavelength squared (see also Kim et al. 2019). The $n\pi$ ambiguity was resolved beforehand, as described in Hovatta et al. (2012). Such large RM values could be produced by the presence of relativistic and thermal electrons in the boundary layer between the jet and the interstellar medium, as reported in Goddi et al. (2021) for the jet in M 87.

3.3. Physical consequences

The high fractional linear polarisation in the innermost region of 3C 84, revealed at 228 GHz, clearly indicates that we are probing a previously elusive region, as we are able to achieve higher resolution while being less affected by opacity effects. We are probing the innermost region of 3C 84 at $\sim 500\,R_{\rm s}$, which appears to be an optically thin region with an ordered magnetic field framing the core.

Furthermore, this region is so compact that an association between the broad jet of 3C 84 and the accretion disk can be ruled out. However, it should be pointed out that both a BH-driven jet and a disc-driven wind could coexist and the present EHT observations are a better probe of the former. In a BH-driven jet scenario, jet launching in 3C 84 might be attributed to a magnetically arrested disc (MAD; see similar simulations carried out for M 87 in Chael et al. 2019), as opposed to a thin, broad disc structure (Liska et al. 2019). Jets in MAD ADAF systems are likely launched by the Blandford–Znajek mechanism Blandford & Znajek (1977), which is the case where a powerful jet spine is powered directly by the energy extracted from the ergosphere of the BH.

Using our estimate of the RM at 228 GHz, it is possible to test whether the magnetic field reaches saturation strength; that is, whether the system is in the MAD state (Narayan et al. 2000; Tchekhovskoy et al. 2011). Under the assumptions described in Appendix E, we find that the dimensionless magnetic flux $\phi = 41 - 93$ (Tchekhovskoy et al. 2011). Values above the saturation value $\phi_{\rm max} = 50$ indicate that the jet is in a magnetically arrested state, and therefore our analysis suggests that jet launching in 3C 84 is MAD. As higher BH spin values and $\beta = 1.5$ produce values close to $\phi_{\rm max}$, our result indicates a preference for a high BH spin and the ADAF model. 3C 84 is also classified as a low-luminosity AGN for which ADAF models are commonly invoked (de Menezes et al. 2020), further strengthening our conclusion. The mass-accretion rate estimated in Appendix E corresponds to $\dot{M} \sim 10^{-5}-10^{-4}\dot{M}_{\rm Edd}$, which is somewhat larger than in the case of M 87 MAD models (see e.g. The Event Horizon Telescope Collaboration 2021b). This suggests that a non-negligible dynamical impact of radiation is possible, which could challenge the applicability of the presented analysis. It should be pointed out here that it is unclear whether Faraday rotation takes place exclusively inside the accretion flow. Our analysis described in Appendix E is based on the assumption that the accretion flow is dominant.

If a spine-sheath geometry (Tavecchio & Ghisellini 2014) is present, manifested in the observations as a transverse

velocity gradient, it could also be the underlying depolarising structure. In this case the rotation of the central BH leads to an inhomogeneous and twisted magnetic field topology (see for example Tchekhovskoy 2015). Furthermore, this scenario would also provide an explanation for the Doppler crisis. As discussed in Hodgson et al. (2021), so-called 'jet-in-jet' formations (Giannios et al. 2009) associated with velocity stratification in the bulk jet flow could be responsible for the enhanced γ-ray emission observed in 3C 84. Such a spine-sheath geometry has already been shown by the EHT to exist on small scales in the jet-launching region of Centaurus A (Janssen et al. 2021).

Ultimately, our detection of the exceptionally high fractional polarisation at 228 GHz, the peculiar jet morphology, and the detailed radio spectrum suggest that the jet in 3C 84 might be launched from both the central BH and the surrounding accretion disc (e.g., Blandford & Globus 2022). As shown by the present findings, millimetre VLBI observations pave the way towards probing the ultimate vicinity of BHs. Future 3C 84 EHT observations with added antennas on short and intermediate baselines will help to constrain the jet morphology and improve the fidelity of the model.

4. Conclusions

In this work we present the first detection of microarcsecond-scale polarised structures with the EHT. Our findings can be summarised as follows:

– We report the first ever 228 GHz VLBI model of 3C 84, which reveals that the compact region is made up of three components.
– We find a high degree of net fractional polarisation $m_{net} = (17.0\pm3.9)\%$. The brightness temperature is $T_b = (3.6\pm1.5)\times 10^{11}$ K, which suggests that the system is in equipartition.
– Using quasi-simultaneous observations of 3C 84 at 15, 43, 86, and 228 GHz, we compute a turnover (optical depth $\tau = 1$) frequency of $\nu_m = (113 \pm 4)$ GHz, a synchrotron self-absorbed magnetic field of $B_{SSA} = (2.9 \pm 1.6)$ G, and an equipartition magnetic field of $B_{eq} = (5.2 \pm 0.6)$ G. However, these values might be influenced by the known variability of the source.
– The increased values of linear polarisation suggest that the observed structure is the approaching jet, which is consistent with the large opening angle. Such a geometry can be produced by a thick disc associated with a Blandford & Znajek (1977) jet-launching scenario.
– We find indications of a preference for higher values of BH spin and the ADAF model in the context of the MAD jet launching prevalent in 3C 84.

The EHT is an excellent instrument for probing AGN cores in nearby radio galaxies. Combined with lower frequency VLBI arrays, such as the GMVA and the VLBA, the EHT makes it possible to conduct multi-frequency studies, which provide valuable insights into jet formation and jet launching. New EHT and GMVA observations have already been carried out, with 3C 84 as the main target. The increased sensitivity and (u, v) coverage will enable us to conduct follow-up studies with higher fidelity. Total intensity images of the compact region will shed more light on whether or not the components we were able to identify here correspond to the broad structure seen with RadioAstron (Giovannini et al. 2018). Spectral index maps of EHT and GMVA images observed quasi-simultaneously might also assist in pinpointing the exact location of the BH (see e.g., Fig. 4 in Paraschos et al. 2022a) and in discriminating between jet launching-scenarios.

References

Abdo, A. A., Ackermann, M., Ajello, M., et al. 2009, ApJ, 699, 31
Agudo, I., Thum, C., Molina, S. N., et al. 2018, MNRAS, 474, 1427
Beck, R., & Krause, M. 2005, Astron. Nachr., 326, 414
Bell, A. R. 1978, MNRAS, 182, 443
Bennett, C. L., Larson, D., Weiland, J. L., & Hinshaw, G. 2014, ApJ, 794, 135
Biermann, P. L., & Strittmatter, P. A. 1987, ApJ, 322, 643
Blackburn, L., Chan, C.-K., Crew, G. B., et al. 2019, ApJ, 882, 23
Blandford, R., & Globus, N. 2022, MNRAS, 514, 5141
Blandford, R. D., & Payne, D. G. 1982, MNRAS, 199, 883
Blandford, R. D., & Znajek, R. L. 1977, MNRAS, 179, 433
Chael, A. A., Johnson, M. D., Narayan, R., et al. 2016, ApJ, 829, 11
Chael, A., Narayan, R., & Johnson, M. D. 2019, MNRAS, 486, 2873
Chamani, W., Savolainen, T., Hada, K., & Xu, M. H. 2021, A&A, 652, A14
Condon, J. J., & Ransom, S. M. 2016, Essential Radio Astronomy (Princeton: Princeton University Press)
de Menezes, R., Nemmen, R., Finke, J. D., Almeida, I., & Rani, B. 2020, MNRAS, 492, 4120
Gardner, F. F., & Whiteoak, J. B. 1966, ARA&A, 4, 245
Giannios, D., Uzdensky, D. A., & Begelman, M. C. 2009, MNRAS, 395, L29
Giovannini, G., Savolainen, T., Orienti, M., et al. 2018, Nat. Astron., 2, 472
Goddi, C., Martí-Vidal, I., Messias, H., et al. 2019, PASP, 131, 075003
Goddi, C., Martí-Vidal, I., Messias, H., et al. 2021, ApJ, 910, L14
Henri, G., & Saugé, L. 2006, ApJ, 640, 185
Hodgson, J. A., Rani, B., Lee, S.-S., et al. 2018, MNRAS, 475, 368
Hodgson, J. A., Rani, B., Oh, J., et al. 2021, ApJ, 914, 43

Hovatta, T., Lister, M. L., Aller, M. F., et al. 2012, AJ, 144, 105
Issaoun, S., Wielgus, M., Jorstad, S., et al. 2022, ApJ, 934, 145
Janssen, M., Goddi, C., van Bemmel, I. M., et al. 2019, A&A, 626, A75
Janssen, M., Falcke, H., Kadler, M., et al. 2021, Nat. Astron., 5, 1017
Jorstad, S. G., Marscher, A. P., Morozova, D. A., et al. 2017, ApJ, 846, 98
Jorstad, S., Wielgus, M., Lico, R., et al. 2023, ApJ, 943, 170
Kim, J. Y., Krichbaum, T. P., Lu, R. S., et al. 2018, A&A, 616, A188
Kim, J. Y., Krichbaum, T. P., Marscher, A. P., et al. 2019, A&A, 622, A196
Kovalev, Y. Y., Lobanov, A. P., Pushkarev, A. B., & Zensus, J. A. 2008, A&A, 483, 759
Kraus, A., Krichbaum, T. P., Wegner, R., et al. 2003, A&A, 401, 161
Li, Y.-P., Yuan, F., & Xie, F.-G. 2016, ApJ, 830, 78
Liska, M., Tchekhovskoy, A., Ingram, A., & van der Klis, M. 2019, MNRAS, 487, 550
Lister, M. L., Aller, M. F., Aller, H. D., et al. 2018, ApJS, 234, 12
Marrone, D. P., Moran, J. M., Zhao, J.-H., & Rao, R. 2006, ApJ, 640, 308
Marscher, A. P. 1983, ApJ, 264, 296
Martí-Vidal, I., Krichbaum, T. P., Marscher, A., et al. 2012, A&A, 542, A107
Martí-Vidal, I., Muller, S., Vlemmings, W., Horellou, C., & Aalto, S. 2015, Science, 348, 311
Martí-Vidal, I., Mus, A., Janssen, M., de Vicente, P., & González, J. 2021, A&A, 646, A52
Mościbrodzka, M., Dexter, J., Davelaar, J., & Falcke, H. 2017, MNRAS, 468, 2214
Myserlis, I., Angelakis, E., Kraus, A., et al. 2018, A&A, 609, A68
Nagai, H., Haga, T., Giovannini, G., et al. 2014, ApJ, 785, 53
Nagai, H., Fujita, Y., Nakamura, M., et al. 2017, ApJ, 849, 52
Narayan, R., & Yi, I. 1995, ApJ, 452, 710
Narayan, R., Igumenshchev, I. V., & Abramowicz, M. A. 2000, ApJ, 539, 798
Oh, J., Hodgson, J. A., Trippe, S., et al. 2022, MNRAS, 509, 1024
Pacholczyk, A. G. 1970, Radio Astrophysics. Nonthermal Processes in Galactic and Extragalactic Sources (San Francisco: Freeman)
Paraschos, G. F., Kim, J. Y., Krichbaum, T. P., & Zensus, J. A. 2021, A&A, 650, L18
Paraschos, G., Kim, J. Y., Krichbaum, T., et al. 2022a, European VLBI Network Mini-Symposium and Users' Meeting, 2021, 43
Paraschos, G. F., Krichbaum, T. P., Kim, J. Y., et al. 2022b, A&A, 665, A1
Paraschos, G. F., Mpisketzis, V., Kim, J. Y., et al. 2023, A&A, 669, A32
Park, J. H., Trippe, S., Krichbaum, T. P., et al. 2015, A&A, 576, L16
Plambeck, R. L., Bower, G. C., Rao, R., et al. 2014, ApJ, 797, 66
Pordes, R., Petravick, D., Kramer, B., et al. 2007, J. Phys. Conf. Ser., 78, 012057P
Punsly, B., Nagai, H., Savolainen, T., & Orienti, M. 2021, ApJ, 911, 19
Rafferty, D. A., McNamara, B. R., Nulsen, P. E. J., & Wise, M. W. 2006, ApJ, 652, 216
Rybicki, G. B., & Lightman, A. P. 1979, Radiative Processes in Astrophysics (New York: Wiley)
Savolainen, T., Wiik, K., Valtaoja, E., & Tornikoski, M. 2008, in Extragalactic Jets: Theory and Observation from Radio to Gamma Ray, eds. T. A. Rector, & D. S. De Young, ASP Conf. Ser., 386, 451
Scharwächter, J., McGregor, P. J., Dopita, M. A., & Beck, T. L. 2013, MNRAS, 429, 2315
Sfiligoi, I., Bradley, D. C., Holzman, B., et al. 2009, WRI World Congress on Computer Science and Information Engineering, 2, 428
Shepherd, M. C., Pearson, T. J., & Taylor, G. B. 1994, Bull. Am. Astron. Soc., 26, 987
Shepherd, M. C., Pearson, T. J., & Taylor, G. B. 1995, Bull. Am. Astron. Soc., 27, 903
Singal, A. K. 1986, A&A, 155, 242
Strauss, M. A., Huchra, J. P., Davis, M., et al. 1992, ApJS, 83, 29
Tavecchio, F., & Ghisellini, G. 2014, MNRAS, 443, 1224
Tchekhovskoy, A. 2015, in The Formation and Disruption of Black Hole Jets, eds. I. Contopoulos, D. Gabuzda, & N. Kylafis, Astrophys. Space Sci. Lib., 414, 45
Tchekhovskoy, A., Narayan, R., & McKinney, J. C. 2010, ApJ, 711, 50
Tchekhovskoy, A., Narayan, R., & McKinney, J. C. 2011, MNRAS, 418, L79
The Event Horizon Telescope Collaboration (Akiyama, K., et al.) 2019a, ApJ, 875, L1
The Event Horizon Telescope Collaboration (Akiyama, K., et al.) 2019b, ApJ, 875, L2
The Event Horizon Telescope Collaboration (Akiyama, K., et al.) 2019c, ApJ, 875, L3
The Event Horizon Telescope Collaboration (Akiyama, K., et al.) 2019d, ApJ, 875, L4
The Event Horizon Telescope Collaboration (Akiyama, K., et al.) 2021a, ApJ, 910, L12
The Event Horizon Telescope Collaboration (Akiyama, K., et al.) 2021b, ApJ, 910, L13
The Event Horizon Telescope Collaboration (Akiyama, K., et al.) 2022a, ApJ, 930, L12
The Event Horizon Telescope Collaboration (Akiyama, K., et al.) 2022b, ApJ, 930, L13
Thompson, A. R., Moran, J. M., Swenson, George W., & J., 2017, Interferometry and Synthesis in Radio Astronomy, 3rd edn. (New York: Springer)
Thum, C., Wiesemeyer, H., Paubert, G., Navarro, S., & Morris, D. 2008, PASP, 120, 777
Türler, M., Courvoisier, T. J. L., & Paltani, S. 2000, A&A, 361, 850
Virtanen, P., Gommers, R., Oliphant, T. E., et al. 2020, Nat. Methods, 17, 261
Wajima, K., Kino, M., & Kawakatu, N. 2020, ApJ, 895, 35
Walker, R. C., Dhawan, V., Romney, J. D., Kellermann, K. I., & Vermeulen, R. C. 2000, ApJ, 530, 233
Wielgus, M., Moscibrodzka, M., Vos, J., et al. 2022, A&A, 665, L6
Zamaninasab, M., Clausen-Brown, E., Savolainen, T., & Tchekhovskoy, A. 2014, Nature, 510, 126

[1] Max-Planck-Institut für Radioastronomie, Auf dem Hügel 69, 53121 Bonn, Germany
e-mail: gfparaschos@mpifr-bonn.mpg.de
[2] Department of Astronomy and Atmospheric Sciences, Kyungpook National University, Daegu 702-701, Republic of Korea
[3] Institute of Physics, Silesian University in Opava, Bezručovo nám. 13, 746 01 Opava, Czech Republic
[4] Instituto de Astrofísica de Andalucía-CSIC, Glorieta de la Astronomía s/n, 18008 Granada, Spain
[5] Institut de Radioastronomie Millimétrique (IRAM), Avenida Divina Pastora 7, Local 20, 18012 Granada, Spain
[6] Department of Astrophysics, Institute for Mathematics, Astrophysics and Particle Physics (IMAPP), Radboud University, PO Box 9010, 6500 GL Nijmegen, The Netherlands
[7] Black Hole Initiative at Harvard University, 20 Garden Street, Cambridge, MA 02138, USA
[8] Center for Astrophysics, Harvard & Smithsonian, 60 Garden Street, Cambridge, MA 02138, USA
[9] Steward Observatory and Department of Astronomy, University of Arizona, 933 N. Cherry Ave., Tucson, AZ 85721, USA
[10] Data Science Institute, University of Arizona, 1230 N. Cherry Ave., Tucson, AZ 85721, USA
[11] Program in Applied Mathematics, University of Arizona, 617 N. Santa Rita, Tucson, AZ 85721, USA
[12] NASA Hubble Fellowship Program, Einstein Fellow, USA
[13] Massachusetts Institute of Technology Haystack Observatory, 99 Millstone Road, Westford, MA 01886, USA
[14] National Astronomical Observatory of Japan, 2-21-1 Osawa, Mitaka, Tokyo 181-8588, Japan
[15] Department of Physics, Faculty of Science, Universiti Malaya, 50603 Kuala Lumpur, Malaysia
[16] Department of Physics & Astronomy, The University of Texas at San Antonio, One UTSA Circle, San Antonio, TX 78249, USA
[17] Institute of Astronomy and Astrophysics, Academia Sinica, 11F of Astronomy-Mathematics Building, AS/NTU No. 1, Sec. 4, Roosevelt Rd., Taipei 10617, Taiwan, R.O.C.
[18] Departament d'Astronomia i Astrofísica, Universitat de València, C. Dr. Moliner 50, 46100 Burjassot, València, Spain
[19] Observatori Astronòmic, Universitat de València, C. Catedrático José Beltrán 2, 46980 Paterna, València, Spain
[20] Department of Space, Earth and Environment, Chalmers University of Technology, Onsala Space Observatory, 43992 Onsala, Sweden
[21] Yale Center for Astronomy & Astrophysics, Yale University, 52 Hillhouse Avenue, New Haven, CT 06511, USA
[22] Department of Physics, University of Illinois, 1110 West Green Street, Urbana, IL 61801, USA
[23] Fermi National Accelerator Laboratory, MS209, PO Box 500, Batavia, IL 60510, USA
[24] Department of Astronomy and Astrophysics, University of Chicago, 5640 South Ellis Avenue, Chicago, IL 60637, USA
[25] East Asian Observatory, 660 N. A'ohoku Place, Hilo, HI 96720, USA
[26] James Clerk Maxwell Telescope (JCMT), 660 N. A'ohoku Place, Hilo, HI 96720, USA

27 California Institute of Technology, 1200 East California Boulevard, Pasadena, CA 91125, USA

28 Institute of Astronomy and Astrophysics, Academia Sinica, 645 N. A'ohoku Place, Hilo, HI 96720, USA

29 Department of Physics and Astronomy, University of Hawaii at Manoa, 2505 Correa Road, Honolulu, HI 96822, USA

30 Department of Physics, McGill University, 3600 rue University, Montréal, QC H3A 2T8, Canada

31 Trottier Space Institute at McGill, 3550 rue University, Montréal, QC H3A 2A7, Canada

32 Institut de Radioastronomie Millimétrique (IRAM), 300 rue de la Piscine, 38406 Saint Martin d'Hères, France

33 Perimeter Institute for Theoretical Physics, 31 Caroline Street North, Waterloo, ON N2L 2Y5, Canada

34 Department of Physics and Astronomy, University of Waterloo, 200 University Avenue West, Waterloo, ON N2L 3G1, Canada

35 Waterloo Centre for Astrophysics, University of Waterloo, Waterloo, ON N2L 3G1, Canada

36 Department of Astronomy, University of Massachusetts, Amherst, MA 01003, USA

37 Korea Astronomy and Space Science Institute, Daedeok-daero 776, Yuseong-gu, Daejeon 34055, Republic of Korea

38 University of Science and Technology, Gajeong-ro 217, Yuseong-gu, Daejeon 34113, Republic of Korea

39 Kavli Institute for Cosmological Physics, University of Chicago, 5640 South Ellis Avenue, Chicago, IL 60637, USA

40 Department of Physics, University of Chicago, 5720 South Ellis Avenue, Chicago, IL 60637, USA

41 Enrico Fermi Institute, University of Chicago, 5640 South Ellis Avenue, Chicago, IL 60637, USA

42 Princeton Gravity Initiative, Jadwin Hall, Princeton University, Princeton, NJ 08544, USA

43 Cornell Center for Astrophysics and Planetary Science, Cornell University, Ithaca, NY 14853, USA

44 Shanghai Astronomical Observatory, Chinese Academy of Sciences, 80 Nandan Road, Shanghai 200030, PR China

45 Key Laboratory of Radio Astronomy, Chinese Academy of Sciences, Nanjing 210008, PR China

46 Physics Department, Fairfield University, 1073 North Benson Road, Fairfield, CT 06824, USA

47 Department of Astronomy, University of Illinois at Urbana-Champaign, 1002 West Green Street, Urbana, IL 61801, USA

48 Instituto de Astronomía, Universidad Nacional Autónoma de México (UNAM), Apdo Postal 70-264, Ciudad de México, Mexico

49 Institut für Theoretische Physik, Goethe-Universität Frankfurt, Max-von-Laue-Straße 1, 60438 Frankfurt am Main, Germany

50 Research Center for Intelligent Computing Platforms, Zhejiang Laboratory, Hangzhou 311100, PR China

51 Tsung-Dao Lee Institute, Shanghai Jiao Tong University, Shengrong Road 520, Shanghai 201210, PR China

52 Department of Astronomy and Columbia Astrophysics Laboratory, Columbia University, 500 W. 120th Street, New York, NY 10027, USA

53 Center for Computational Astrophysics, Flatiron Institute, 162 Fifth Avenue, New York, NY 10010, USA

54 Dipartimento di Fisica "E. Pancini", Universitá di Napoli "Federico II", Compl. Univ. di Monte S. Angelo, Edificio G, Via Cinthia, 80126 Napoli, Italy

55 INFN Sez. di Napoli, Compl. Univ. di Monte S. Angelo, Edificio G, Via Cinthia, 80126 Napoli, Italy

56 Wits Centre for Astrophysics, University of the Witwatersrand, 1 Jan Smuts Avenue, Braamfontein, Johannesburg 2050, South Africa

57 Department of Physics, University of Pretoria, Hatfield, Pretoria 0028, South Africa

58 Centre for Radio Astronomy Techniques and Technologies, Department of Physics and Electronics, Rhodes University, Makhanda 6140, South Africa

59 ASTRON, Oude Hoogeveensedijk 4, 7991 PD Dwingeloo, The Netherlands

60 LESIA, Observatoire de Paris, Université PSL, CNRS, Sorbonne Université, Université de Paris, 5 place Jules Janssen, 92195 Meudon, France

61 JILA and Department of Astrophysical and Planetary Sciences, University of Colorado, Boulder, CO 80309, USA

62 National Astronomical Observatories, Chinese Academy of Sciences, 20A Datun Road, Chaoyang District, Beijing 100101, PR China

63 Las Cumbres Observatory, 6740 Cortona Drive, Suite 102, Goleta, CA 93117-5575, USA

64 Department of Physics, University of California, Santa Barbara, CA 93106-9530, USA

65 National Radio Astronomy Observatory, 520 Edgemont Road, Charlottesville, VA 22903, USA

66 Department of Electrical Engineering and Computer Science, Massachusetts Institute of Technology, 32-D476, 77 Massachusetts Ave., Cambridge, MA 02142, USA

67 Google Research, 355 Main St., Cambridge, MA 02142, USA

68 Institut für Theoretische Physik und Astrophysik, Universität Würzburg, Emil-Fischer-Str. 31, 97074 Würzburg, Germany

69 Department of History of Science, Harvard University, Cambridge, MA 02138, USA

70 Department of Physics, Harvard University, Cambridge, MA 02138, USA

71 NCSA, University of Illinois, 1205 W. Clark St., Urbana, IL 61801, USA

72 Instituto de Astronomia, Geofísica e Ciências Atmosféricas, Universidade de São Paulo, R. do Matão, 1226, São Paulo, SP 05508-090, Brazil

73 Dipartimento di Fisica, Universitá degli Studi di Cagliari, SP Monserrato-Sestu km 0.7, 09042 Monserrato, (CA), Italy

74 INAF – Osservatorio Astronomico di Cagliari, Via della Scienza 5, 09047 Selargius (CA), Italy

75 INFN, sezione di Cagliari, 09042 Monserrato (CA), Italy

76 CP3-Origins, University of Southern Denmark, Campusvej 55, 5230 Odense M, Denmark

77 Instituto Nacional de Astrofísica, Óptica y Electrónica. Apartado Postal 51 y 216, 72000 Puebla Pue., Mexico

78 Consejo Nacional de Ciencia y Tecnología, Av. Insurgentes Sur 1582, 03940 Ciudad de México, México

79 Key Laboratory for Research in Galaxies and Cosmology, Chinese Academy of Sciences, Shanghai 200030, PR China

80 Mizusawa VLBI Observatory, National Astronomical Observatory of Japan, 2-12 Hoshigaoka, Mizusawa, Oshu, Iwate 023-0861, Japan

81 Department of Astronomical Science, The Graduate University for Advanced Studies (SOKENDAI), 2-21-1 Osawa, Mitaka, Tokyo 181-8588, Japan

82 Trottier Space Institute at McGill, 3550 rue University, Montréal, QC H3A 2A7, Canada

83 NOVA Sub-mm Instrumentation Group, Kapteyn Astronomical Institute, University of Groningen, Landleven 12, 9747 AD Groningen, The Netherlands

84 Department of Astronomy, School of Physics, Peking University, Beijing 100871, PR China

85 Kavli Institute for Astronomy and Astrophysics, Peking University, Beijing 100871, PR China

86 Department of Astronomy, Graduate School of Science, The University of Tokyo, 7-3-1 Hongo, Bunkyo-ku, Tokyo 113-0033, Japan

87 The Institute of Statistical Mathematics, 10-3 Midori-cho, Tachikawa, Tokyo 190-8562, Japan

88 Department of Statistical Science, The Graduate University for Advanced Studies (SOKENDAI), 10-3 Midori-cho, Tachikawa, Tokyo 190-8562, Japan

89 Kavli Institute for the Physics and Mathematics of the Universe, The University of Tokyo, 5-1-5 Kashiwanoha, Kashiwa 277-8583, Japan

[90] Leiden Observatory, Leiden University, Postbus 2300, 9513 RA Leiden, The Netherlands

[91] ASTRAVEO LLC, PO Box 1668, Gloucester, MA 01931, USA

[92] Applied Materials Inc., 35 Dory Road, Gloucester, MA 01930, USA

[93] Institute for Astrophysical Research, Boston University, 725 Commonwealth Ave., Boston, MA 02215, USA

[94] Institute for Cosmic Ray Research, The University of Tokyo, 5-1-5 Kashiwanoha, Kashiwa, Chiba 277-8582, Japan

[95] Joint Institute for VLBI ERIC (JIVE), Oude Hoogeveensedijk 4, 7991 PD Dwingeloo, The Netherlands

[96] Kogakuin University of Technology & Engineering, Academic Support Center, 2665-1 Nakano, Hachioji, Tokyo 192-0015, Japan

[97] Graduate School of Science and Technology, Niigata University, 8050 Ikarashi 2-no-cho, Nishi-ku, Niigata 950-2181, Japan

[98] Physics Department, National Sun Yat-Sen University, No. 70, Lien-Hai Road, Kaosiung City 80424, Taiwan, R.O.C.

[99] National Optical Astronomy Observatory, 950 N. Cherry Ave., Tucson, AZ 85719, USA

[100] Department of Physics, The Chinese University of Hong Kong, Shatin, N. T., Hong Kong

[101] School of Astronomy and Space Science, Nanjing University, Nanjing 210023, PR China

[102] Key Laboratory of Modern Astronomy and Astrophysics, Nanjing University, Nanjing 210023, PR China

[103] INAF-Istituto di Radioastronomia, Via P. Gobetti 101, 40129 Bologna, Italy

[104] INAF-Istituto di Radioastronomia & Italian ALMA Regional Centre, Via P. Gobetti 101, 40129 Bologna, Italy

[105] Department of Physics, National Taiwan University, No. 1, Sec. 4, Roosevelt Rd., Taipei 10617, Taiwan, R.O.C.

[106] Instituto de Radioastronomía y Astrofísica, Universidad Nacional Autónoma de México, Morelia 58089, Mexico

[107] Yunnan Observatories, Chinese Academy of Sciences, 650011 Kunming, Yunnan Province, PR China

[108] Center for Astronomical Mega-Science, Chinese Academy of Sciences, 20A Datun Road, Chaoyang District, Beijing 100012, PR China

[109] Key Laboratory for the Structure and Evolution of Celestial Objects, Chinese Academy of Sciences, 650011 Kunming, PR China

[110] Anton Pannekoek Institute for Astronomy, University of Amsterdam, Science Park 904, 1098 XH Amsterdam, The Netherlands

[111] Gravitation and Astroparticle Physics Amsterdam (GRAPPA) Institute, University of Amsterdam, Science Park 904, 1098 XH, Amsterdam, The Netherlands

[112] Department of Astrophysical Sciences, Peyton Hall, Princeton University, Princeton, NJ 08544, USA

[113] Science Support Office, Directorate of Science, European Space Research and Technology Centre (ESA/ESTEC), Keplerlaan 1, 2201 AZ Noordwijk, The Netherlands

[114] School of Physics and Astronomy, Shanghai Jiao Tong University, 800 Dongchuan Road, Shanghai 200240, PR China

[115] Astronomy Department, Universidad de Concepción, Casilla 160-C, Concepción, Chile

[116] National Institute of Technology, Hachinohe College, 16-1 Uwanotai, Tamonoki, Hachinohe City, Aomori 039-1192, Japan

[117] Research Center for Astronomy, Academy of Athens, Soranou Efessiou 4, 115 27 Athens, Greece

[118] Department of Physics, Villanova University, 800 Lancaster Avenue, Villanova, PA 19085, USA

[119] Physics Department, Washington University, CB 1105, St. Louis, MO 63130, USA

[120] School of Physics, Georgia Institute of Technology, 837 State St NW, Atlanta, GA 30332, USA

[121] Department of Astronomy and Space Science, Kyung Hee University, 1732, Deogyeong-daero, Giheung-gu, Yongin-si, Gyeonggi-do 17104, Republic of Korea

[122] Canadian Institute for Theoretical Astrophysics, University of Toronto, 60 St. George Street, Toronto, ON M5S 3H8, Canada

[123] Dunlap Institute for Astronomy and Astrophysics, University of Toronto, 50 St. George Street, Toronto, ON M5S 3H4, Canada

[124] Canadian Institute for Advanced Research, 180 Dundas St West, Toronto, ON M5G 1Z8, Canada

[125] Radio Astronomy Laboratory, University of California, Berkeley, CA 94720, USA

[126] Institute of Astrophysics, Foundation for Research and Technology – Hellas, Voutes 7110, Heraklion, Greece

[127] Department of Physics, National Taiwan Normal University, No. 88, Sec. 4, Tingzhou Rd., Taipei 116, Taiwan, R.O.C.

[128] Center of Astronomy and Gravitation, National Taiwan Normal University, No. 88, Sec. 4, Tingzhou Road, Taipei 116, Taiwan, R.O.C.

[129] Finnish Centre for Astronomy with ESO, University of Turku, 20014 Turku, Finland

[130] Aalto University Metsähovi Radio Observatory, Metsähovintie 114, 02540 Kylmälä, Finland

[131] Gemini Observatory/NSF NOIRLab, 670 N. A'ohōkūPlace, Hilo, HI 96720, USA

[132] Frankfurt Institute for Advanced Studies, Ruth-Moufang-Strasse 1, 60438 Frankfurt, Germany

[133] School of Mathematics, Trinity College, Dublin 2, Ireland

[134] Department of Physics, University of Toronto, 60 St. George Street, Toronto, ON M5S 1A7, Canada

[135] Department of Physics, Tokyo Institute of Technology, 2-12-1 Ookayama, Meguro-ku, Tokyo 152-8551, Japan

[136] Hiroshima Astrophysical Science Center, Hiroshima University, 1-3-1 Kagamiyama, Higashi-Hiroshima, Hiroshima 739-8526, Japan

[137] Aalto University Department of Electronics and Nanoengineering, PL 15500, 00076 Aalto, Finland

[138] Department of Astronomy, Yonsei University, Yonsei-ro 50, Seodaemun-gu 03722, Seoul, Republic of Korea

[139] National Biomedical Imaging Center, Peking University, Beijing 100871, PR China

[140] College of Future Technology, Peking University, Beijing 100871, PR China

[141] Department of Physics and Astronomy, University of Lethbridge, Lethbridge, Alberta T1K 3M4, Canada

[142] Netherlands Organisation for Scientific Research (NWO), Postbus 93138, 2509, AC Den Haag, The Netherlands

[143] Department of Physics and Astronomy, Seoul National University, Gwanak-gu, Seoul 08826, Republic of Korea

[144] University of New Mexico, Department of Physics and Astronomy, Albuquerque, NM 87131, USA

[145] Jeremiah Horrocks Institute, University of Central Lancashire, Preston PR1 2HE, UK

[146] Physics Department, Brandeis University, 415 South Street, Waltham, MA 02453, USA

[147] Tuorla Observatory, Department of Physics and Astronomy, University of Turku, Turku, Finland

[148] Radboud Excellence Fellow of Radboud University, Nijmegen, The Netherlands

[149] School of Natural Sciences, Institute for Advanced Study, 1 Einstein Drive, Princeton, NJ 08540, USA

[150] School of Physics, Huazhong University of Science and Technology, Wuhan, Hubei 430074, PR China

[151] Mullard Space Science Laboratory, University College London, Holmbury St. Mary, Dorking, Surrey RH5 6NT, UK

[152] School of Astronomy and Space Sciences, University of Chinese Academy of Sciences, No. 19A Yuquan Road, Beijing 100049, PR China

[153] Astronomy Department, University of Science and Technology of China, Hefei 230026, PR China

[154] Department of Physics and Astronomy, Michigan State University, 567 Wilson Rd, East Lansing, MI 48824, USA

Appendix A: Additional methodology comments

The frequency setup of the EHT in 2017 consisted of two bands, each of 2 GHz in width, centred at 227.1 GHz (LO band) and 229.1 GHz (HI band): see The Event Horizon Telescope Collaboration (2019b) for details. For all the presented analyses, we combined data sets from both bands, using data points averaged over 2 GHz in frequency and for 120 s in time. In the EHT data sets, the polarimetric calibration relies on the calibration of ALMA (Goddi et al. 2019), which provides the absolute EVPA and serves as a reference site for the computation of the complex polarimetric gains for the entire EHT array (The Event Horizon Telescope Collaboration 2021a). As ALMA was present in only one-sixth of the observing scans of 3C 84, we only obtained the ALMA-based calibration for the single scan. The corresponding EVPA measurement on the short ALMA-APEX baseline is close to the north–south axis, consistent with POLAMI observations. This is in contrast to previous polarimetric analyses with the EHT (The Event Horizon Telescope Collaboration 2021a; Issaoun et al. 2022; Jorstad et al. 2023), where the absolute EVPA reference was always constrained by ALMA. As a consequence, the absolute EVPA calibration was found to be challenging and dependent on additional assumptions for the remaining part of the observations, with the additional difficulties related to APEX drop-outs in the HI band and JCMT observing only the right-hand circular polarisation component, which was used as as proxy for the total intensity in a similar way to in the previous EHT analyses (e.g. The Event Horizon Telescope Collaboration 2019a, 2022a). Hence, in the fitting to the linearly polarised source structure, we made a choice to only fit the absolute values of the fractional Fourier polarisation (corresponding to $|\breve{m}|$, the amplitude ratio of cross-hand and parallel-hand visibility components, following the notation of The Event Horizon Telescope Collaboration 2021a), as shown in the right panel of Fig. A.1. We therefore neglect the corrupted linear polarisation phase information. As a consequence, we only interpret the absolute values of fractional polarisation of the fitted Gaussian components. In astrophysical synchrotron plasma, the following order of Stokes parameters magnitude is generally expected: $I > |P| \gg V$; circular polarisation V is consequently neglected in the studies of total intensity I and linear polarisation P. Under this assumption, we can use single-polarisation JCMT data in the fitting to absolute values of Fourier fractional linear polarisation.

The high quality of the fit is quantified with the reduced χ^2, which is provided in Fig. A.1 for different data products used for the simultaneous fitting: visibility amplitudes, closure phases, and fractional Fourier linear polarisation (see e.g. The Event Horizon Telescope Collaboration 2021a, for the exact definition). Additionally, in Fig. A.2, the closure phases observed on the APEX-SMT-JCMT triangle are compared with our model (model 3g, with three Gaussian components representing the compact region emission). Non-zero closure phases are an immediate indication of a resolved structure, inconsistent with a circular symmetry of the source (Thompson et al. 2017).

The dominant systematic uncertainty in the linear polarisation analysis results comes from the lack of the polarimetric leakage calibration (D-terms calibration; The Event Horizon Telescope Collaboration 2021a), which could not be directly employed for the 3C 84 data set, given the aforementioned data set issues pertaining to the uncertain, time-dependent EVPA calibration. In order to obtain a rough characterisation of the impact of the leakage on the resulting polarimetric quantities, we performed a small survey of data sets calibrated with different D-terms. We assumed the magnitude of the complex EHT array D-terms estimated and verified in previous EHT publications (The Event Horizon Telescope Collaboration 2021a; Issaoun et al. 2022; Jorstad et al. 2023), but generated ten random realisations of D-term phases, subsequently refitting the polarimetric source model to data sets with different leakage calibration variants. The fractional polarisation uncertainties reported in Table A.1 reflect the results of the D-term calibration survey.
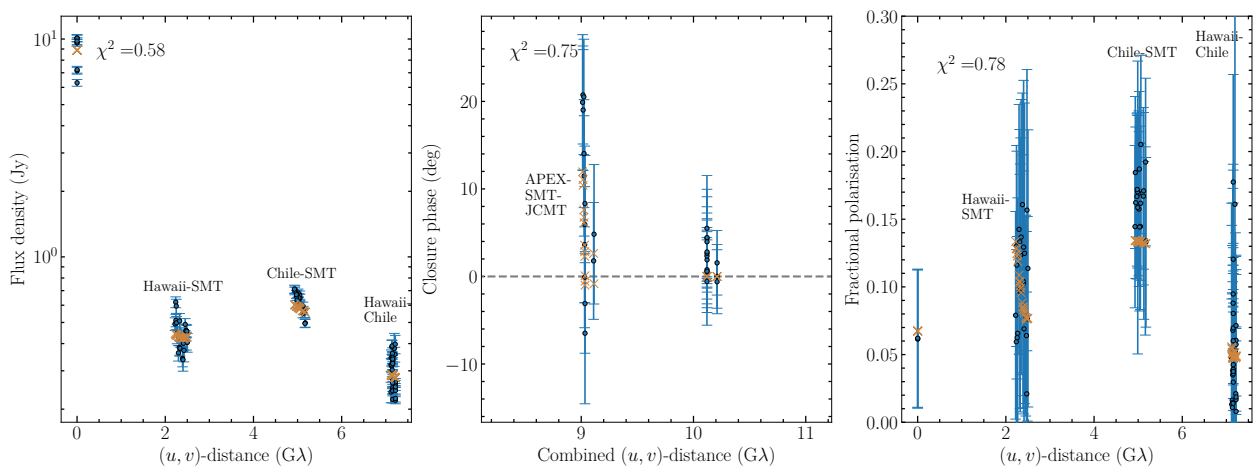
Fig. A.1. Best-fit model of 3C 84 compared to the data. Presented here from left to right are the data points (denoted with round blue markers) and models (denoted with dark orange crosses) of the visibility amplitudes, closure phases, and fractional polarisation as a function of the (u, v) distance. The combined (u, v) distance used in the middle panel is defined as the square root of the sum of squared lengths of all three baselines forming a triangle. Error bars in all panels indicate the 68% confidence level.

Table A.1. Summary of the image parameters

Frequency [GHz]	ID	Flux density [Jy]	T_B [10^{10} K]	FWHM [μas]	Polarisation [%]	Position [μas, μas]
15	E+C+W	1.77	253.7 ± 76.3	62.1 ± 8.1	<2.0	(0.0, 0.0)
43	E	0.07	3.6 ± 1.5	35.5 ± 7.1	<7.0	(34.4, -20.1)
	C	1.69	411.4 ± 175.8	16.6 ± 3.3	<1.0	(0.0, 0.0)
	W	0.80	535.5 ± 228.8	10.0 ± 2.0	<2.0	(-26.1, -8.58)
86	E	1.49	19.8 ± 8.4	35.5 ± 7.1	<1.0	(34.4, -20.1)
	C	3.06	186.2 ± 79.5	16.6 ± 3.3	<1.0	(0.0, 0.0)
	W	0.58	97.6 ± 41.7	10.0 ± 2.0	<2.0	(-26.1, -8.58)
228	E	0.93	1.8 ± 0.8	35.5 ± 7.1	20.0 ± 5.8	(34.4, -20.1)
	C	1.02	8.8 ± 3.8	16.6 ± 3.3	11.0 ± 2.0	(0.0, 0.0)
	W	0.04	1.0 ± 0.4	10.0 ± 2.0	40.0 − 80.0	(-26.1, -8.58)

At 15 GHz the image resolution is insufficient to confidently distinguish between the compact region components, and so we limit ourselves to reporting the integrated flux density and fractional polarisation values instead. The positional uncertainty is of the order of $\leq 2\%$ for E in the east–west and north–south directions, and $\leq 7\%$ in the east–west and $\leq 60\%$ in north–south direction for W. Here, C is fixed at (0, 0). The uncertainties of the flux density measurements are of the order of 20% at 15 GHz, 30% at 43 GHz, 50% at 86 GHz, and 15% at 228 GHz (The Event Horizon Telescope Collaboration 2019c). The large relative uncertainty in the fractional polarisation of W is related to its small total flux density. The FWHM and positions of the 43, 86, and 228 GHz components have been fixed in the multi-frequency template-matching framework. Error margins indicate the 68% confidence level.
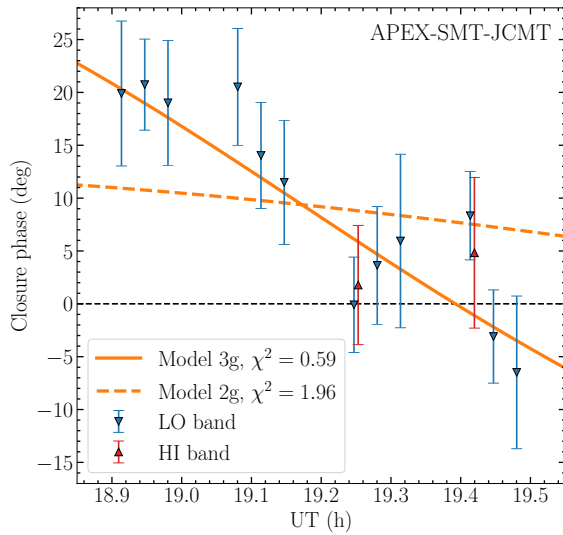
Fig. A.2. Closure phases as a function of the time of observation, detected on the APEX-SMT-JCMT non-trivial triangle, compared with the predictions of the model presented in this paper. Error bars indicate the 68% confidence level. The best-fit model 2g with two Gaussian components representing the compact emission region fails to adequately capture the trend in the data, unlike the 3g model with three components. The reported χ^2 corresponds to the non-trivial subset of all measured closure phases.

Table A.2. Extended flux measurements

Frequency [GHz]	Flux [Jy]
8	40.1 ± 8.5*
86	22.2 ± 1.1**
228	10.9 ± 0.55**

*QUIVER (Effelsberg 100m Telescope)
**POLAMI (IRAM 30m Telescope)

Appendix B: Modelling the EHT data
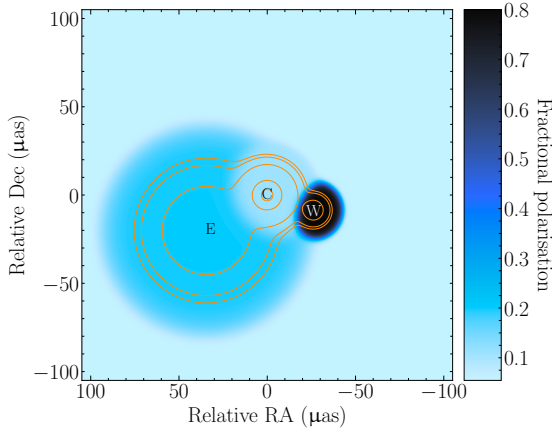
Fig. B.1. Fractional polarisation image. Shown here is a representation of the best-fit model to the fractional polarisation data in the image plane. Contours correspond to 0.5, 1, 5, 50, and 90% of the peak brightness temperature $T_b = 3.6 \times 10^{11}$ K. We note the high net fractional linear polarisation of $m_{net} = (17.0 \pm 3.9)\%$ in the compact region probed by the EHT.

We modelled the EHT data with circular Gaussian components, because the (u, v) coverage is too sparse to reconstruct an image from it. Circular instead of elliptical Gaussian components were preferred in order to reduce the number of degrees of freedom. We used the forward modelling `eht-imaging` software (Chael et al. 2016) and leveraged heuristic optimisation tools implemented in `SciPy` (Virtanen et al. 2020) to search for the best-fit solution in terms of a minimum of an error function. Figure A.1 presents our best-fit model to the visibility amplitudes, closure phases, and fractional polarisation as a function of the (u, v) distance. Figure B.1 shows the fractional polarisation of the best-fit solution. See Appendix A for additional comments on the fitting procedure.

A certain degree of ambiguity in the compact source structure and the number of components is expected due to the large asymmetry of the EHT (u, v) coverage, which provides resolving power primarily along the south–east/north–west axis; see Fig. 1. In particular, we considered the choice between a two-component (2g) and a three-component (3g) model of the compact emission. The former corresponds to ten geometric degrees of freedom (i.e., not counting the amplitude gains) for the compact emission and three for the extended emission. The latter adds six degrees of freedom to the compact emission part. While in the data set used for fitting there are 86 visibility amplitudes, 14 non-trivial closure phases (all shown in Fig. A.2), and 80 absolute values of fractional linear polarisations, there are strong correlations between data points in time, frequency, and location on the (u, v) plane. The presence of such correlations reduces the effective constraining power of the data set. Hence, the model selection becomes a non-trivial problem. The best-fit 2g model essentially recovers the presented geometry of E and C components with the same fractional polarisation of C and around 35% polarisation of E. While the 2g model fits the amplitudes and fractional polarisations well, it is not capable of reproducing the closure phase measurements in a joint fit to all data products, which we demonstrate in Fig. A.2. This, along with earlier results obtained at lower observing frequencies (Punsly et al. 2021), motivates the selection of the 3g model for the presented analysis, despite it being slightly over-fitted according to the χ^2

values reported in Fig. A.1. Such behaviour is generally expected for an accurate model given the strong correlations present in the data.

Appendix C: Multi-frequency template matching

We used circular Gaussian components to model the EHT data, determining the number of degrees of freedom required to accurately fit visibility amplitudes, closure phases, and fractional Fourier polarisation, including the modelling of station-based, time-dependent amplitude gains. This is made possible by using the template-matching technique (e.g. Savolainen et al. 2008; Kovalev et al. 2008), which leverages prior knowledge of the source's brightness distribution from high-frequency measurements (here 228 GHz) to estimate the source structure at lower frequencies, even if they are closer together than the lower frequency beam size. Given sufficient S/N, structures smaller than the diffraction-limited interferometric resolution can be constrained (e.g. Martí-Vidal et al. 2012). For our observations, $S/N \sim 550$ at 43 GHz and $S/N \sim 375$ at 86 GHz, resulting in nominal resolution limits $d_{lim}^{43\,GHz} = 19\,\mu as$ and $d_{lim}^{86\,GHz} = 6\,\mu as$, respectively. Therefore, we were able to apply the high-frequency template, given that the separation between the components comprising the template was sufficiently large. It should be noted here, that these calculations are performed under the assumption that the source's morphology is a Gaussian. However, given the complex structure in the compact region of 3C 84 revealed here, the actual resolution may be worse. We therefore adopted the more conservative approach of restricting the resolution limit to the typical value of approximately one-fifth of the beam size (e.g. Oh et al. 2022). This was still possible in our case at 43 GHz (beam size $\sim 100\,\mu as$) and 86 GHz (beam size $\sim 50\,\mu as$). As in our work we investigate the overall spectral behaviour of the submas region, this approach is sufficient to get an estimate for the flux densities and fractional polarisations for each component. We also disregarded the core shift effects (see e.g. Paraschos et al. 2021; Oh et al. 2022; Paraschos et al. 2023) between the images at different frequencies, because their effect is negligible for our analysis (of the order of a few tens of μas). Our results are summarised in Table A.1. The uncertainties of the flux density measurements are on the order of 20% at 15 GHz, 30% at 43 GHz, 50% at 86 GHz, and 15% at 228 GHz (The Event Horizon Telescope Collaboration 2019c).

Appendix D: Magnetic field estimate

We estimated the magnetic field strength in the core via synchrotron turnover frequency fitting. The synchrotron spectrum takes the following form (Condon & Ransom 2016):

$$S(\nu) = S_0 \left(\frac{\nu}{\nu_1}\right)^{\alpha_{thick}} \left\{1 - \exp\left[-\left(\frac{\nu}{\nu_1}\right)^{-(p+4)/2}\right]\right\}, \quad (D.1)$$

for a homogeneous and cylindrical source, where ν_1 is the frequency where the opacity reaches unity, $\tau = 1$, and $S_0 = 5.7 \pm 0.3$ Jy is a multiplication constant, determined from the fit. Subsequently, ν_m is calculated by determining the peak of the fitted spectrum. Following Kim et al. (2019), we set $\alpha_{thick} = 0.51 \pm 0.10$. The parameter p is the power-law slope of the electron energy distribution function and is set to $p = 2$ (Condon & Ransom 2016).

We used two different prescriptions for the magnetic field strength. First we calculated the equipartition magnetic field B_{eq}

using Pacholczyk ([1970](#)) with the following form[2]:

$$
\left(\frac{B_{eq}}{G}\right) = 2.7 \times 10^{-7}
$$

$$
\left[\frac{(1+k_u)\,c_{12}\kappa_\nu}{f}\,\frac{S_m/Jy}{(\theta/mas)^3}\,\frac{\nu_m/Hz}{D_L/Gpc}\,\frac{(1+z)^{10}}{\delta^4}\right]^{2/7}. \quad (D.2)
$$

We note that the exponent 2/7 only holds for $\alpha_{thin} = 0.5$ (see Beck & Krause [2005](#), for a relevant discussion). Here, k_u is a ratio that provides an estimate of the energy in relativistic protons compared to electrons and f is a factor denoting the fraction of the total volume of the emitting region occupied by the plasma and magnetic field in equipartition. Under the assumption of an electron-positron pair plasma (see Paraschos et al. [2023](#), for a discussion about electron-positron pair plasma in the vicinity of the SMBH in 3C 84), which is volume filling, $k_u = 0$ and $f = 1$. The uncertainties for k_u and f are difficult to constrain; their impact on the magnetic field strength computation is discussed below. The constant c_{12} (in cgs units) is given by the following expression:

$$
c_{12} = c_1^{1/2} c_2^{-1} \left(\frac{2+2\alpha_{thick}}{1+2\alpha_{thick}}\right) \left(\frac{\nu_{min}^{(1+2\alpha_{thick})/2} - \nu_{max}^{(1+2\alpha_{thick})/2}}{\nu_{min}^{1+\alpha_{thick}} - \nu_{max}^{1+\alpha_{thick}}}\right), \quad (D.3)
$$

where $c_1 = \frac{3e}{4\pi m_e^3 c^5} = 6.27 \times 10^{18}$ [cgs] and $c_2 = \frac{2e^4}{3m_e^4 c^7} = 2.37 \times 10^{-3}$ [cgs]; e and m_e are the charge and mass of the electron respectively and c is the speed of light. Furthermore, κ_ν is defined as

$$
\kappa_\nu \equiv \frac{(\nu_{max}/\nu_m)^{1+\alpha_{thick}} - 1}{1+\alpha_{thick}}\,\frac{(\nu_{min}/\nu_m)^{1+\alpha_{thin}} - 1}{1+\alpha_{thin}}, \quad (D.4)
$$

where ν_{min} and ν_{max} are the minimum and maximum frequency range of synchrotron radiation. We used $\nu_{min} = 10^7$ Hz (lowest possible frequency for synchrotron emission) and $\nu_{max} = 3 \times 10^{14}$ Hz (Biermann & Strittmatter [1987](#)). As $[\nu_{min}, \nu_{max}]$ constitute an assumed frequency range, their values are presented without uncertainties. The optically thin spectral index is $\alpha_{thin} = -0.5$ (Kim et al. [2019](#)). The angular diameter is denoted as θ and the synchrotron peak flux density as $S_m = 9.0 \pm 0.5$ Jy at the frequency ν_m, extrapolated from the optically thin flux density (see also Chamani et al. [2021](#)). We assumed $\delta = 1.1 \pm 0.1$ for the Doppler factor based on observations presented in Kim et al. ([2019](#)), Punsly et al. ([2021](#)), Paraschos et al. ([2021](#)) and used $\theta = (144 \pm 18)\,\mu$as (this value already includes the geometric correction discussed in Marscher ([1983](#))).

Additionally, using Eq. 2 in Marscher ([1983](#)):

$$
\left(\frac{B_{SSA}}{G}\right) = 10^{-50} b(\alpha_{thin}) \left(\frac{\theta}{mas}\right)^4 \left(\frac{\nu_m}{Hz}\right)^5 \left(\frac{S_m}{Jy}\right)^{-2} \left(\frac{\delta}{1+z}\right). \quad (D.5)
$$

Our choice of $\alpha_{thin} = -0.5$ results in $b(\alpha_{thin}) = 3.2$. The resulting estimates for the magnetic field are $B_{SSA} = (2.9 \pm 1.6)$ G and $B_{eq} = (5.2 \pm 0.6)$ G for the core component C at 228 GHz. We point out that the B_{SSA} calculation is strongly impacted by the value of ν_m. An increase or decrease of a few GHz would vary the value of B_{SSA} by two orders of magnitude. Similarly, the B_{eq} calculation strongly depends on the assumption of k_u, that is, the particle composition of the jet. Alternative assumptions of the jet composition resulting in an increase in k_u (diffusive shock acceleration would result in values of $k_u \lesssim 50$, see e.g. Bell [1978](#))

---

[2] Here, we assume equipartition between cosmic-ray and magnetic energy density.

would increase the value of B_{eq} by up to a factor of 3. Likewise, decreasing the value of f (assuming a clumpier medium, filling only half of the total emitting region for example), would result in an increase in B_{eq} by a factor of 1.2. However, we note that the good agreement between the two magnetic field estimates indicates that the choice of $k_u = 0$ and $f = 1$ is reasonable. The equipartition Doppler factor required for B_{SSA} to match B_{eq} is $\delta_{eq} = 1.5 \pm 0.4$.

Finally, we can compare B_{eq} and B_{SSA} to the strength of the coherent field based on the observed RM. Using Eq. 15 from Gardner & Whiteoak ([1966](#)), written:

$$
RM = 8.1 \times 10^5 \int n_e B_\parallel^{tot} dl, \quad (D.6)
$$

we can compute the lower limit of the strength of the ordered field, $B_\parallel^{tot}$. Here, n_e is the number density of the thermal electrons, which we set to $n_e = 3 \times 10^4\,cm^{-3}$ (Scharwächter et al. [2013](#)). The path length of integration through the plasma is dl and can be approximated by $\psi \times \theta$. Using these values, $B_\parallel^{tot} = 4.7 \pm 0.6$ mG, which is consistent as a lower limit to our calculations of B_{eq} and B_{SSA}.

Appendix E: Dimensionless magnetic flux

We calculated the dimensionless magnetic flux ϕ using the expression for the jet power P_{jet} Tchekhovskoy et al. ([2010](#)), which holds for black hole spin values $\alpha_* \leq 1$:

$$
\left(\frac{P_{jet}}{\dot{M}c^2}\right) = \frac{\kappa}{4\pi}\phi^2\Omega_H^2\left[1 + 1.38\Omega_H^2 - 9.2\Omega_H^4\right]. \quad (E.1)
$$

Here, $\Omega_H \equiv \frac{|\alpha_*|}{2(1+\sqrt{1-\alpha_*^2})}$, $\dot{M}$ is the mass-accretion rate of 3C 84, and $\kappa = 0.05$ is a constant depending on the initial field geometry.

To determine the mass-accretion rate, we use Eq. 9 from Marrone et al. ([2006](#)), in the following form (as also shown in Nagai et al. [2017](#)):

$$
\left(\frac{\dot{M}}{M_\odot\,yr^{-1}}\right) = 1.3 \times 10^{-10}\left(1 - \left(\frac{r_{out}}{r_{in}}\right)^{-(3\beta-1)/2}\right)^{-2/3}
$$

$$
\left(\frac{M_{BH}}{8.0 \times 10^8\,M_\odot}\right)^{4/3}\left(\frac{2}{3\beta-1}\right)^{-2/3} r_{in}^{7/6}\left(\frac{RM}{rad\,m^{-2}}\right)^{2/3}. \quad (E.2)
$$

where $\beta = 0.5$ for CDAF or $\beta = 1.5$ for ADAF and r_{in} and r_{out} are the inner and outer effective radii of the accretion flow. Furthermore, $\dot{M}_{Edd} = L_{Edd}/(\epsilon c^2)$, where ϵ is an efficiency factor. Using $L_{Edd} \sim 10^{47}\,erg\,s^{-1}$ (Plambeck et al. [2014](#)), $\epsilon = 0.1$, $r_{out} \sim 10^5\,R_s$ (Nagai et al. [2017](#)), $r_{in} \sim 90\,R_s$ (size of C), and $RM = (6.06 \pm 0.01) \times 10^6\,rad\,m^{-2}$ yields $\dot{M} = 0.3 \times 10^{-3}\,M_\odot\,yr^{-1}$ for $\beta = 0.5$ and $\dot{M} \sim 1.1 \times 10^{-3}\,M_\odot\,yr^{-1}$ $\beta = 1.5$. This computation rests on the assumption that the Faraday screen is external. Our assumption is physically motivated; the jet viewing angle used in our computations ($\xi \sim 40°$) is larger than half of the intrinsic jet opening angle ($i \lesssim 20°$; see e.g. Paraschos et al. [2021](#)), suggesting that we are peering through the jet sheath and boundary layer (see also Plambeck et al. [2014](#); Nagai et al. [2017](#)). Furthermore, at 1.3 mm, we are able to directly examine the environment of the central engine, because the opacity effects become comparatively minor.

Finally, the total luminosity of the jet in 3C 84 (Rafferty et al. [2006](#)) is $P_{jet} = 1.5 \times 10^{44}\,erg\,s^{-1}$. Thus, setting $a_* = $

1, we computed a range of $\phi = 41 - 93$. Values of $\phi \gtrsim 50$ refer to MAD models (Tchekhovskoy et al. 2011; Zamaninasab et al. 2014). We note here that the RM would need to be underestimated by more than an order of magnitude (e.g. due to the Faraday screen not being external) for ϕ to equal its MAD saturation value. Our investigation of different flow geometries and black hole spins supports an advection-dominated accretion flow in a magnetically arrested state as a model of the jet launching system in the core of 3C 84.